Properties of the Ellipse-Line-Ellipse Trajectory with Asymmetrical Variations

Zijia Guo[a,b], Frédéric Noo[a], Andreas Maier[b], Guenter Lauritsch[c]

[a]Utah Center for Advanced Imaging Research, Department of Radiology and Imaging Sciences, University of Utah, USA
[b]Pattern Recognition Lab, University of Erlangen-Nuremberg, Germany
[c]Siemens Healthcare GmbH, Germany

ABSTRACT

Three-dimensional cone-beam (CB) imaging using a multi-axis floor-mounted (or ceiling-mounted) C-arm system has become an important tool in interventional radiology. This success motivates new developments to improve image quality. One direction in which advancement is sought is the data acquisition geometry and related CB artifacts. Currently, data acquisition is performed using the circular short-scan trajectory, which yields limited axial coverage and also provides incomplete data for accurate reconstruction. To improve the image quality, as well as to increase the coverage in the longitudinal direction of the patient, we recently introduced the ellipse-line-ellipse trajectory and showed that this trajectory provides full R-line coverage within the field-of-view, which is a key property for accurate reconstruction from truncated data. An R-line is any segment of line that connects two source positions. Here, we examine how the application of asymmetrical variations to the definition of the ELE trajectory impacts the R-line coverage. This question is significant to understand how much flexibility can be used in the implementation of the ELE trajectory, particularly to adapt the scan to patient anatomy and imaging task of interest. Two types of asymmetrical variations, called axial and angular variations, are investigated.

1. INTRODUCTION

Three-dimensional cone-beam (CB) imaging using a multi-axis floor-mounted (or ceiling-mounted) C-arm system has become an important tool in interventional radiology (see e.g.[1–6]). This tool helps physicians plan more effective interventions, reduces treatment-related complications, and enables the development of novel minimally-invasive surgical procedures, which is not only beneficial for the patient but also reduces financial costs. These attractive features motivate a continuous effort towards technological advances that aim at improving the quality of images.

One direction in which advancement is sought is the data acquisition geometry and related CB artifacts. Currently, data acquisition is performed using the circular short-scan trajectory, which yields limited axial coverage and also provides incomplete data for accurate reconstruction. To improve the image quality, as well as to increase the coverage in the longitudinal direction of the patient, it is needed to move away from the circular short-scan trajectory. Fortunately, many data acquisition geometries are now feasible, thanks to the increase in the range of motions offered by some multi-axis robotic mounted C-arm systems. For example, the multi-axis Artis Zeego system (Siemens Healthcare GmbH, Forchheim, Germany) offers eight degrees of freedom in motion, as illustrated in Figure 1. Using such a system, we recently demonstrated the ability to acquire data and perform reconstruction using a reverse helix as the source trajectory.[7]

An important constraint applied to the data acquisition geometry is that it should allow accurate image reconstruction from truncated data, while being mechanically practical. In terms of modern CB reconstruction algorithms, this constraint means that the source trajectory should provide full R-line coverage. An R-line is any line that connects two points on the source trajectory. Each point within the field-of-view (FOV) should belong to an R-line. Unfortunately, this property is not satisfied by the reverse helix,[8] so that accurate and practical image reconstruction with this trajectory has remained elusive.

Medical Imaging 2016: Physics of Medical Imaging, edited by Despina Kontos, Thomas G. Flohr, Joseph Y. Luo,
Proc. of SPIE Vol. 9783, 97832Z · © 2016 SPIE · CCC code: 1605-7422/16/$18 · doi: 10.1117/12.2217187

Figure 1: Multi-axis Artis Zeego system (Siemens Healthcare GmbH, Forchheim, Germany), which offers eight degrees of freedom in motion for data acquisition. These degrees of freedom are highlighted by red arrows.

Recently, we introduced a novel practical data acquisition geometry, the ellipse-line-ellipse (ELE) trajectory.[9] The R-lines properties of this trajectory have been extensively studied, and it has been found that the ELE trajectory offers full R-line coverage.[9,10] Additionally, reconstruction algorithms that are dedicated to this geometry have been developed and successfully tested on simulated data, with competitive detector size requirements.[10,11] Here, we are interested in examining how the application of asymmetrical variations to the definition of the ELE trajectory impacts the R-line coverage. This question is significant to understand how much flexibility can be used in the implementation of the ELE trajectory, particularly to adapt the scan to patient anatomy and imaging task of interest. We investigate two types of asymmetrical variations, called axial and angular variations.

2. BACKGROUND

The ELE trajectory consists of two tilted elliptical arcs (called T-arcs, where T stands for trajectory) and a segment of line (called T-line) that connects them. The T-line is in the longitudinal direction of the patient, whereas the T-arcs are in planes that are nearly orthogonal to this direction. See Figure 2 for an illustration.

As illustrated, the ELE trajectory lies on a cylinder of radius R centered on a z-axis that corresponds to the long axis of the patient. The three points, O, O_+ and O_-, on the z-axis represent the origin and the center of the T-arcs. The T-arc centered on $O+$ is called the upper T-arc, whereas the other one is called the lower T-arc. Any point on a T-arc is described with a polar angle λ that varies between $-\gamma_m$ and $\pi+\gamma_m$, where γ_m is a given angle. In Cartesian coordinates, (x, y, z), the components of a point on a T-arc are

$$(R\cos\lambda, R\sin\lambda, \mathcal{H}_{1,2}(\lambda)) \tag{1}$$

where $\mathcal{H}_1(\lambda) = H + \Delta H\cos\lambda$ for the upper T-arc and $\mathcal{H}_2(\lambda) = -(H + \Delta H\cos\lambda)$ for the lower T-arc. Parameter $\Delta H \in (0, H)$ controls the tilt magnitude of the T-arcs, whereas H specifies the distance in z between the origin and the center of each T-arc.

A more convenient notation is obtained by normalizing ΔH relative to H. Let $d = \Delta H/H$. Then, a source point on a T-arc can be expressed as

$$(R\cos\lambda, R\sin\lambda, \pm H\,(1 + d\cos\lambda)) \tag{2}$$

When $d = 0$, the T-arcs lie in planes that are orthogonal to the z-axis, but the ELE trajectory does not provide full R-line coverage in this configuration, unless $\gamma_m = \pi/2$. Given the limitations of mounted C-arms in terms of angular motion, it is however preferable to have $2\gamma_m$ much closer to the minimum fan angle that covers the FOV, which is pictured as a cylinder of radius r centered on the z-axis (or more precisely the portion thereof that is between the two T-arcs).

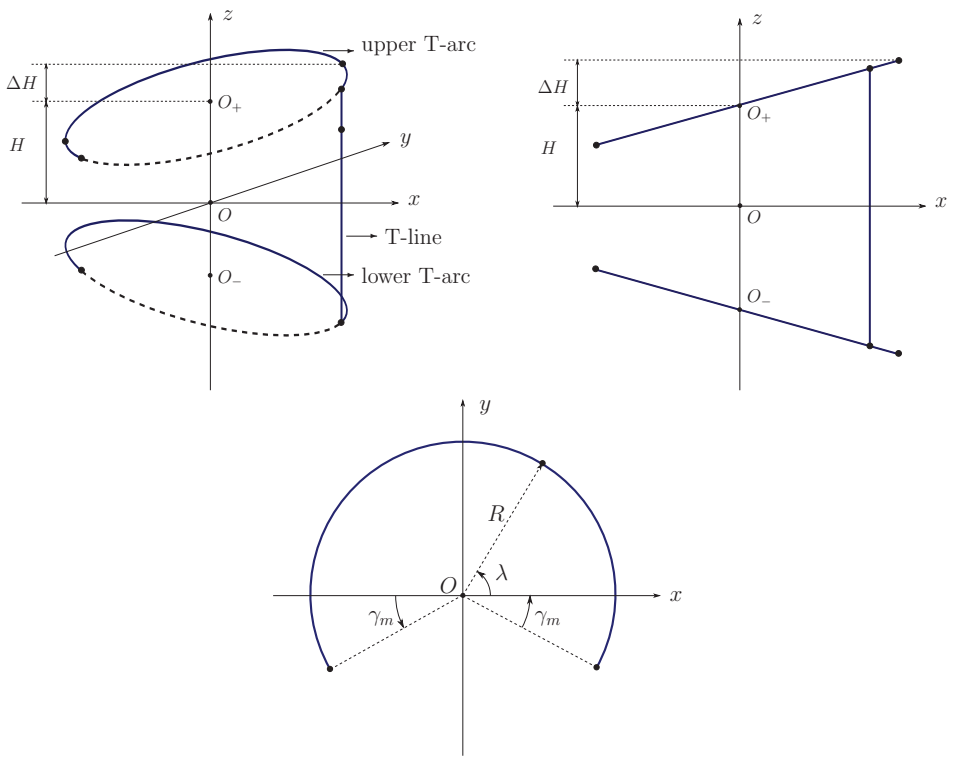

Figure 2: ELE trajectory. Top left: in 3D; the z-axis is in the longitudinal direction of the patient. Top right: projection onto the (x, z) plane. Bottom: projection onto the (x, y) plane.

R-line coverage for the ELE trajectory can be examined on a slice-by-slice basis, using slices that are orthogonal to the z-axis. Consider any given such slice, and assume that an R-line intersects this slice, then the intersection point is one location within the slice where R-line coverage exists. If we pick a point on the upper T-arc and connect it successively with each point on the lower T-arc, we get a set of R-lines that create, by intersection, a segment of ellipse in any given slice. Such a segment of ellipse is called an AA R-arc, where AA stands for T-arc to T-arc. The union of AA R-arcs obtained by varying the point on the upper T-arc gives, within the slice, the R-line coverage that is associated with any R-line joining a point on the upper T-arc to a point on the lower T-arc. Figure 3 (left) shows a number of AA R-arcs in slice $z = 0.25\,H$, all in red.

To identify all points that are covered by R-lines within a given slice, we also need to consider the coverage associated with R-lines that connect a point on the T-line to a point on a T-arc. This coverage is identified by two special R-arcs, called AL R-arcs, where AL stands for T-arc to T-line. The first AL R-arc comes from the R-lines that connect the point at $\lambda = -\gamma_m$ on the upper T-arc to all points on the lower T-arc. The second AL R-arc comes from the R-lines that connect the point at $\lambda = -\gamma_m$ on the lower T-arc to all points on the upper T-arc. The convex hull of each of these AL R-arcs corresponds to points covered by R-lines that connect a point on the T-line to a point on a T-arc. Figure 3 (middle) shows the two AL R-arcs in slice $z = 0.25\,H$, both in black. Figure 3 (right) shows the entire R-line coverage within slice $z = 0.25\,H$, as obtained when considering all possible R-lines, with grayscale color coding indicating the number of R-lines passing through each location.

An interesting aspect for the ELE trajectory is that R-line coverage within the FOV can be examined by simply evaluating the coverage in slice $z = 0$. If the FOV is fully covered by R-lines in that plane, then the whole 3D FOV is covered by R-lines. This property is a consequence of the symmetry of the trajectory. Figure 4 shows a set of AA R-arcs contributing to the coverage in slice $z = 0$, as well as the two AL R-arcs, and the resulting total coverage. This figure corresponds to parameters such that the FOV, drawn as a blue circle, is fully covered. Note that there is only one AL R-arc visible in slice $z = 0$, because the two AL R-arcs in this plane are identical to each other. Note also that the AA R-arcs all share a common point in slice $z = 0$; the coordinates of this point can be shown to be $(-R\,d, 0, 0)$. Finally, for future reference, note that we call the region of missing coverage

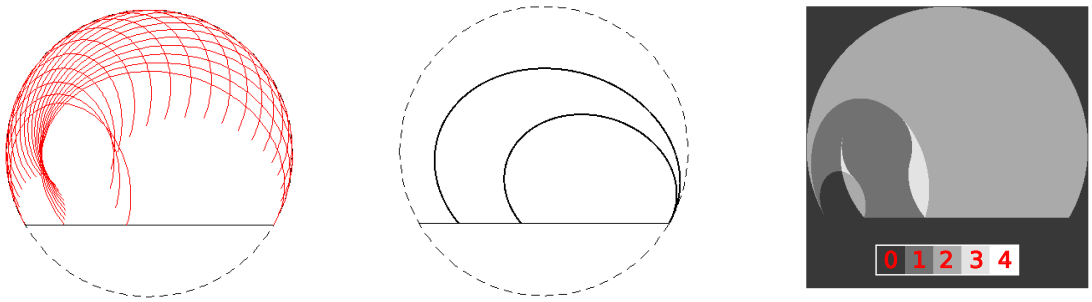

Figure 3: R-line coverage in a plane orthogonal to the z-axis. See section 2 for details.

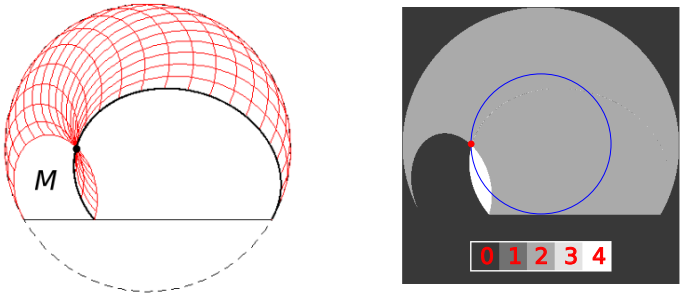

Figure 4: R-line coverage in the central plane, $z = 0$. See section 2 for details.

in slice $z = 0$ as region M; this region, marked in Figure 4 (left), is bounded by three curves, specifically it is bounded below by line $y = -R \sin \gamma_m$, bounded on the left by an AA R-arc, and bounded on the right by the AL R-arc.

Mathematical analysis based on the observations in Figure 4 yields the following theorem characterizing the R-line coverage for the ELE trajectory:[9]

> *The ELE trajectory yields full R-line coverage of the FOV when parameters γ_m and d are such that $\gamma_m \geq \arcsin(r/R)$ and $d \geq r/R$ together with $r/R < 0.85$.*

3. ASYMMETRICAL VARIATIONS

We examine two asymmetrical variations in the definition of the ELE trajectory: axial variations, which refer to asymmetrical settings along the z-axis, and angular variations, which refer to changes in the projection view on the (x, y) plane. These variations are first analyzed independently of each other. However, a thorough analysis will reveal that they can be jointly considered.

3.1 Axial Variations

The axial variations under consideration correspond to using different values for H and ΔH in the description of the upper and lower T-arcs. The upper T-arc is now characterized by values H_1 and ΔH_1, whereas the lower T-arc is characterized by values H_2 and ΔH_2, as illustrated in figure 5. Using a coordinate transformation that amounts to a translation in z by $(H_1 - H_2)/2$, we immediately notice that, without loss of generality, the axial variations can be analyzed under the assumption that $H_1 = H_2$, i.e., axial variations can be entirely expressed using ΔH_1 and ΔH_2. Indeed, R-line coverage is invariant under such a transformation. Hereafter, H_1 and H_2 are denoted as H. We assume that $\Delta H_{1,2} \in (0, H)$, and we introduce $d_1 = \Delta H_1/H$ and $d_2 = \Delta H_2/H$, as well as $\bar{d} = (d_1 + d_2)/2$ and $\Delta d = (d_2 - d_1)/2$.

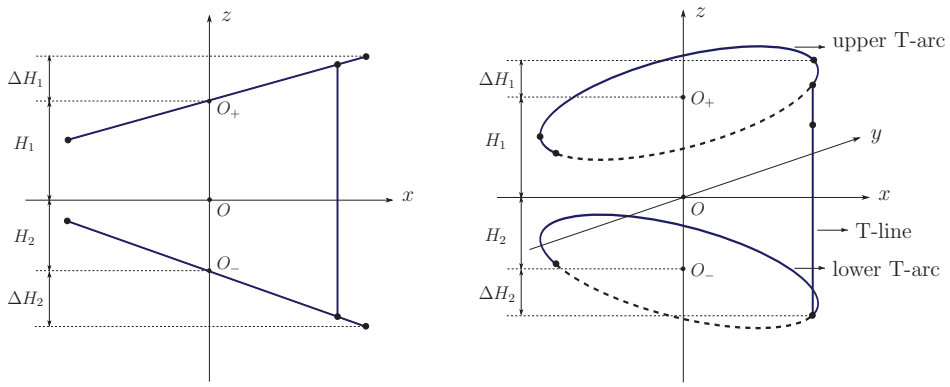

Figure 5: ELE trajectory with axial variations. (left) Projection onto the (x, z) plane. (right) 3D view. Compare with Fig. 2.

3.2 Angular Variations

The angular variations under consideration correspond to using a different expression for the starting and ending angles on the upper and lower T-arcs. We now assume that $\lambda \in [-\gamma_1, \pi + \gamma_2]$, where $\gamma_{1,2} \in [0, \pi/2)$, and γ_1 and γ_2 need not be equal, as shown in figure 6. Note that this angular variation causes a change in the positioning of the T-line, which could be useful for some applications. For convenience, we introduce $\bar{\gamma} = (\gamma_1 + \gamma_2)/2$ and $\Delta\gamma = (\gamma_2 - \gamma_1)/2$. We assume that $\bar{\gamma} \geq \arcsin(r/R)$, which is a minimum requirement to ensure data completeness. By construction, the following inequalities hold: $\bar{\gamma} > 0$, $|\Delta\gamma| \leq \bar{\gamma}$, and $|\Delta\gamma| \leq \pi/2 - \bar{\gamma}$.

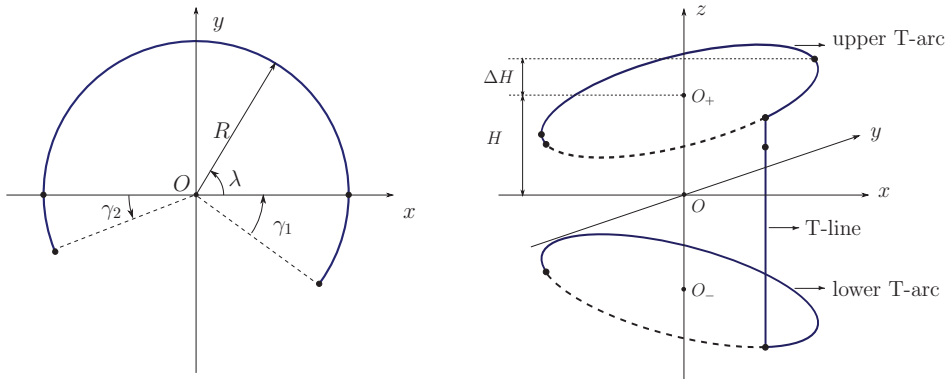

Figure 6: ELE trajectory with angular variations. (left) Projection of the trajectory onto the (x, y) plane. (right) 3D view. Compare with Fig. 2 and notice how the angular variations affect the position of the T-line.

3.3 R-line coverage with asymmetrical axial variations

As with the classical ELE trajectory, R-line coverage can be investigated on a slice-by-slice basis, using slices orthogonal to the z-axis. Results of such an investigation are shown hereafter. They allow appreciating differences, but do not unfortunately lead to a theorem on coverage of the FOV as straightforwardly as in.[9,10] Indeed, a complication arises from the fact the trajectory is not mirror-symmetric about the (x, y) plane when axial variations are present. Hence, examining coverage in slice $z = 0$ is not sufficient anymore.

First, we inspected the arrangement of AA and AL R-arcs in slice $z = 0$. This inspection highlighted a first major difference: the R-arcs do not anymore share a common point in slice $z = 0$ when $\Delta H_1 \neq \Delta H_2$. In fact, the arrangement of the R-arcs in this slice appears more similar to the arrangement observed in a slice $z \neq 0$ when $\Delta H_1 = \Delta H_2$. We then varied z and observed that there actually still exists a z-slice where the AA R-arcs share a common point when $\Delta H_1 \neq \Delta H_2$. The position of this slice can be shown to be $z = e_c\, H$ with $e_c = \bar{d}\,\Delta d$, and the coordinates of the common point are $(-R\,\bar{d}, 0, e_c\, H)$. A second major difference we observed is that the AL R-arcs are not such that one is embedded in (and tangent to) the other one when $\Delta H_1 \neq \Delta H_2$, and

there does not seem to exist any z-location where they overlap. Figure 7 shows the arrangement of AA and AL R-arcs in slices $z = \{0, 0.5\,e_c, e_c, 2\,e_c\}H$, and the resulting coverage of R-lines in these slices. These results convey that, even though important differences can be observed, the FOV may remain fully covered by R-lines when $\Delta H_1 \neq \Delta H_2$.

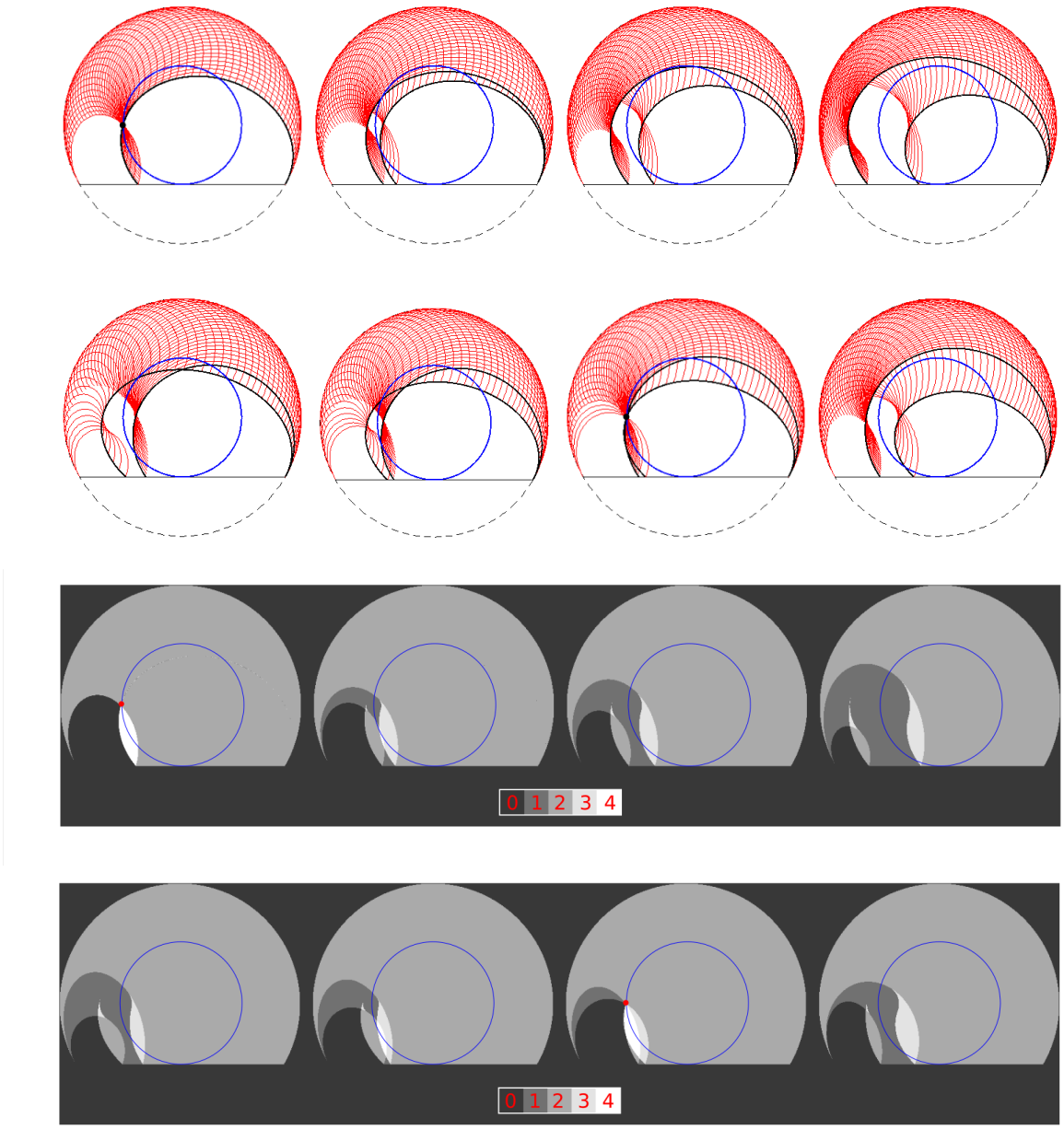

Figure 7: Comparison of R-line coverage in slice $z = eH$ without and with axial variations. First and third row: results without axial variations. Second and last row: results with axial variations. From left to right: $e = 0$, $e = 0.5\,e_c$, $e = e_c$, $e = 2\,e_c$. For this illustration, we used $\gamma_m = \pi/6$, $\bar{d} = 0.5$ and $e_c \triangleq \bar{d}\,\Delta d = 0.125$.

We have found a mathematical methodology to analyze the R-line coverage with axial variations. This methodology will be reported in a future publication. It shows that R-line coverage is guaranteed when parameters γ_m and $\bar{d}$ are such that $\gamma_m \geq \arcsin(r/R)$ and $\bar{d} \geq r/R$ together with $r/R < 0.85$. Thus, we can state that great flexibility exists in terms of axial variations.

3.4 R-line coverage with asymmetrical angular variations

Here, we assume that $\Delta H_1 = \Delta H_2$. However, it is possible to show that the results below also apply to $\Delta H_1 \neq \Delta H_2$ if d is replaced by $\bar{d}$. Under the assumption that $\Delta H_1 = \Delta H_2$, we can prove as in the classical case that it is only necessary to analyze coverage in slice $z = 0$.

Figure 8 illustrates the arrangement of AA and AL R-arcs in slice $z = 0$ for $\bar{\gamma} = \pi/6$ and also for $\bar{\gamma} = \pi/4$. In each case, the arrangements are shown for five different choices of $\Delta\gamma$. This illustration conveys that R-line coverage is affected by the values chosen for γ_1 and γ_2: the portion of the AL R-arc that contributes to the boundary of region M (i.e., the region where there is no R-line coverage) moves towards the FOV as γ_1 is decreased.

Figure 9 shows the whole R-line coverage in slice $z = 0$ for the extreme case where $\gamma_1 = 0$, in comparison with the case where $\gamma_1 = \gamma_2$. The coverage is shown for both cases, $\bar{\gamma} = \pi/6$ and $\bar{\gamma} = \pi/4$, assuming the radius of the FOV is $R \sin\bar{\gamma}$. In the case where $\bar{\gamma} = \pi/4$, we observe that using $\gamma_1 = 0$ results in a situation where the FOV is not fully covered by R-lines. Hence, new careful analysis is required to understand which parameters are acceptable.

We have found that to the method used in [9,10] to evaluate the coverage can be generalized to account for angular variations. Detailed explanations will be reported in a future publication, along with our results on axial variations. Based on this generalization, it appears that $\arcsin(r/R) \leq \bar{\gamma} \leq \pi/6$ with $d = r/R$ is sufficient to guarantee full R-line coverage of the FOV. Although this condition is fairly restricting on r/R, relative to the case where $\Delta\gamma = 0$, it is equivalent to the geometry of a diagnostic CT scanner and thus practical.

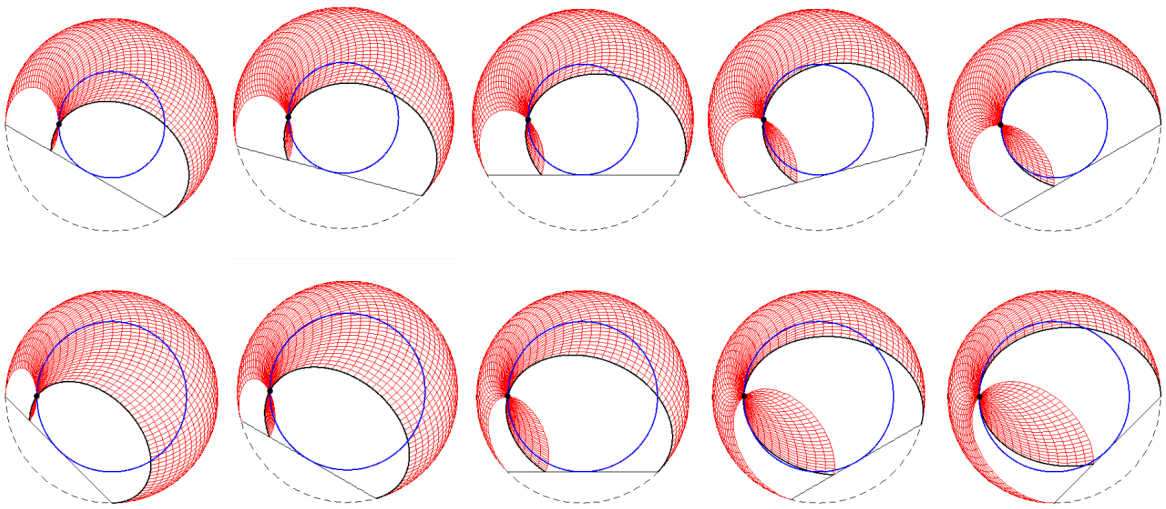

Figure 8: R-line coverage with angular variations. AA and AL R-arcs are shown in slice $z = 0$ for various choices of $\Delta\gamma$, with the FOV drawn as a blue circle. Top row: $\bar{\gamma} = \pi/6$ with $\Delta\gamma = -\pi/6$, $-\pi/12$, 0, $\pi/12$, $\pi/6$ from left to right. Bottom row: $\bar{\gamma} = \pi/4$ with $\Delta\gamma = -\pi/4$, $-\pi/6$, 0, $\pi/6$, $\pi/4$ from left to right. In both cases, the radius of the FOV is $R \sin\bar{\gamma}$.

4. DISCUSSION

We have examined R-line coverage for modified versions of the ELE trajectory that include asymmetrical variations. Both axial and angular variations were considered. We have found that a large flexibility exists in the configuration of the ELE trajectory without impacting the R-line coverage. This feature further reinforces attractiveness of this trajectory for long object imaging in interventional radiology.

5. DISCLAIMER

The concepts presented in this paper are based on research and are not commercially available.

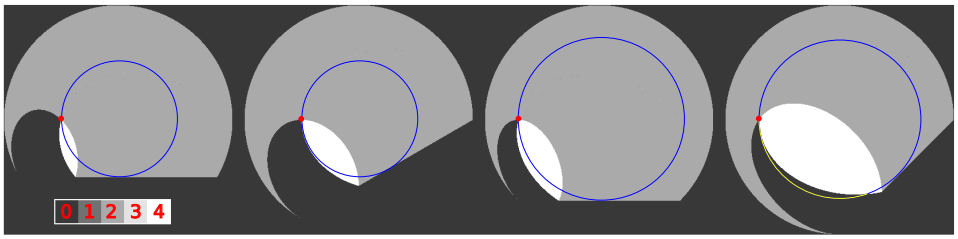

Figure 9: R-line coverage in slice $z = 0$ with angular variations. From left to right: $\bar{\gamma} = \pi/6$ with $\gamma_1 = \gamma_2$; $\bar{\gamma} = \pi/6$ with $\gamma_1 = 0$; $\bar{\gamma} = \pi/4$ with $\gamma_1 = \gamma_2$; $\bar{\gamma} = \pi/4$ with $\gamma_1 = 0$.

6. ACKNOWLEDGMENT

This work was partly supported by the Erlangen Graduate School in Advanced Optical Technologies (SAOT); the authors gratefully acknowledge funding of SAOT by the German Research Foundation (DFG) in the framework of the German excellence initiative.

REFERENCES

[1] Binkert, C., Alencar, H., Singh, J., and Baum, R., "Translumbar type II endoleak repair using angiographic CT," *J Vasc Interv Radiol* **17**(8), 1349–1353 (2006).

[2] Hodek-Wuerz, R., Martin, J., Wilhelm, K., Lovblad, K., Babic, D., Rufenacht, D., and Wetzel, S., "Percutaneous vertebroplasty: preliminary experiences with rotational acquisitions and 3D reconstructions for therapy control," *Cardiovasc Inter Rad* **29**(5), 862–865 (2006).

[3] Meyer, B., Frericks, B., Albrecht, T., Wolf, K., and Wacker, F., "Contrast-enhanced abdominal angiographic CT for intra-abdominal tumor embolization: a new tool for vessel and soft tissue visualization," *Cardiovasc Inter Rad* **30**(4), 743–749 (2007).

[4] Wallace, M., Kuo, M., Glaiberman, C., Binkert, C., Orth, R., and Soulez, G., "Three-dimensional C-arm cone-beam CT: applications in the interventional suite," *J Vasc Interv Radiol* **19**(6), 799–813 (2008).

[5] Wong, A. A., Charalel, R. A., Louie, J. D., and Sze, D. Y., "Carbon dioxide contrast enhancement for C-arm CT utility for treatment planning during hepatic embolization procedures," *J Vasc Interv Radiol* **24**(7), 975–980 (2013).

[6] Lightfoot, C. B., Ju, Y., Dubois, J., Abdolell, M., Giroux, M.-F., Gilbert, P., Therasse, E., Oliva, V., and Soulez, G., "Cone-beam CT: An additional imaging tool in the interventional treatment and management of low-flow vascular malformations," *J Vasc Interv Radiol* **24**(7), 981–988 (2013).

[7] Yu, Z., Maier, A., Lauritsch, G., Vogt, F., Schonborn, M., Kohler, C., Hornegger, J., and Noo, F., "Axially extended-volume C-arm CT using a reverse helical trajectory in the interventional room," *Medical Imaging, IEEE Transactions on* **34**(1), 203–215 (2015).

[8] Cho, S., Xia, D., Pelizzari, C. A., and Pan, X., "Exact reconstruction of volumetric images in reverse helical cone-beam CT," *Med. Phys.* **35**, 3030–3040 (Jul. 2008).

[9] Yu, Z., Lauritsch, G., Dennerlein, F., Mao, Y., Hornegger, J., and Noo, F., "Extended ellipse-line-ellipse trajectory for long-object cone-beam imaging with a mounted C-arm system," *Physics in medicine and biology* **61**(4), 1829 (2016).

[10] Yu, Z., *C-arm Computed Tomography with Extended Axial Field-of-View*, PhD thesis, Friedrich-Alexander-Universität Erlangen-Nürnberg (2013).

[11] Yu, Z., Lauritsch, G., Hornegger, J., and Noo, F., "Efficient and exact C-arm cone-beam imaging for axially extended field-of-view using the ellipse-line-ellipse trajectory," in [*Proceedings of The 3rd International Conference on Image Formation in X-Ray Computed Tomography*], 311–314 (Jun. 2014).